FINAL REPORT

Project Title: University of Nevada Reno Photo-electrochemical Project

Award No.: DE-FC36-06 GO86066

Project Location: Materials Science and Engineering
University of Nevada, Reno
Reno, NV, 89557-0388

Subcontractor: Chemistry Department
University of Nevada Las Vegas

Reporting Period: Final Report

Date of Report: December 20, 2014

Project Contacts: Dev Chidambaram

DOE Technology Development Manager:
Eric L. Miller
Fuel Cell Technologies
202-287-5829
eric.miller@ee.doe.gov

DOE Project Officer:
David Peterson
Phone: (303) 275-4956;
Fax: (303) 275-4788
David.Peterson@go.doe.gov

FINAL REPORT

Project Title: University of Nevada, Reno Photo-Electrochemical Project

Objective:

- Develop high efficiency metal oxide nanotubular array photo-anodes for generating hydrogen by water splitting;
- Develop density functional theory to understand the effect of the morphology of the nanotubes on the photo-electrochemical (PEC) properties of the photo-anodes;
- Develop kinetics and formation mechanism of the metal oxide nanotubes under different synthesis conditions;
- Develop combinatorial approach to prepare hybrid photo-anodes having multiple hetero-atoms incorporation in a single photo anode;
- Improve the durability of the material; and
- Scale up the laboratory demonstration to production unit

Most of the work conducted under this award has been published and those publications are attached as in print form. The unpublished progress that was conducted in last 6 months are provided below.

Publications Resulting from this award:

[1] R. Gakhar, A. Merwin, K. Summers, S. K. Pilli, and D. Chidambaram, "Application of ZnxCd1-xSe-sensitized TiO2 nanotube arrays as photoanodes for solar cells," Journal of Materials Chemistry A, vol. 2, pp. 10116-10125, Jul 14 2014.

[2] R. Gakhar, K. Summers, R. Palaniappan, S. K. Pilli, and D. Chidambaram, "Sensitization of TiO2 nanotube array photoelectrodes with MnxCdySe," Rsc Advances, vol. 4, pp. 49729-49736, 2014 2014.

[3] Y. R. Smith, R. Gakhar, A. Merwin, S. K. Mohanty, D. Chidambaram, and M. Misra, "Anodic Titania Nanotube Arrays Sensitized with Mn- or Co-Doped CdS Nanocrystals," Electrochimica Acta, vol. 135, pp. 503-512, Jul 20 2014.

[4] B. Sarma, R. S. Ray, S. K. Mohanty, and M. Misra, "Synergistic enhancement in the capacitance of nickel and cobalt based mixed oxide supercapacitor prepared by electrodeposition," Applied Surface Science, vol. 300, pp. 29-36, May 1 2014.

[5] B. Sarma, A. L. Juroyitzki, Y. R. Smith, R. S. Ray, and M. Misra, "Influence of annealing temperature on the morphology and the supercapacitance behavior of iron oxide nanotube (Fe-NT)," Journal of Power Sources, vol. 272, pp. 766-775, Dec 25 2014.

[6] B. Sarma, Y. R. Smith, A. L. Jurovitzki, R. S. Ray, S. K. Mohanty, and M. Misra, "Supercapacitance behavior of porous oxide layer grown on 302 type stainless steel substrate," Journal of Power Sources, vol. 236, pp. 103-111, Aug 15 2013.

[7] Y. R. Smith, R. S. Ray, K. Carlson, B. Sarma, and M. Misra, "Self-Ordered Titanium Dioxide Nanotube Arrays: Anodic Synthesis and Their Photo/Electro-Catalytic Applications," Materials, vol. 6, pp. 2892-2957, Jul 2013.

[8] B. Sarma, A. L. Jurovitzki, Y. R. Smith, S. K. Mohanty, and M. Misra, "Redox-Induced Enhancement in Interfacial Capacitance of the Titania Nanotube/Bismuth Oxide Composite Electrode," Acs Applied Materials & Interfaces, vol. 5, pp. 1688-1697, Mar 13 2013.

[9] Y. R. Smith, B. Sarma, S. K. Mohanty, and M. Misra, "Light-Assisted Anodized TiO2 Nanotube Arrays," Acs Applied Materials & Interfaces, vol. 4, pp. 5883-5890, Nov 2012.

[10] Y. R. Smith, S. K. Mohanty, and M. Misra, "Formation of WO3-TiO2 nanotubular composite via single-step anodization and its application in photoelectrochemical hydrogen generation," Abstracts of Papers of the American Chemical Society, vol. 243, Mar 25 2012.

[11] Y. R. Smith, B. Sarma, S. K. Mohanty, and M. Misra, "Formation of TiO2-WO3 nanotubular composite via single-step anodization and its application in photoelectrochemical hydrogen generation," Electrochemistry Communications, vol. 19, pp. 131-134, Jun 2012.

[12] B. Sarma, Y. R. Smith, S. K. Mohanty, and M. Misra, "Electrochemical deposition of CdO on anodized TiO2 nanotube arrays for enhanced photoelectrochemical properties," Materials Letters, vol. 85, pp. 33-36, Oct 15 2012.

[13] S. Banerjee, S. K. Mohapatra, and M. Misra, "Water Photooxidation by TiSi2-TiO2 Nanotubes," Journal of Physical Chemistry C, vol. 115, pp. 12643-12649, Jun 30 2011.

[14] S. Banerjee, M. Misra, S. K. Mohapatra, C. Howard, S. K. Mohapatra, and S. K. Kamilla, "Formation of chelating agent driven anodized TiO2 nanotubular membrane and its photovoltaic application," Nanotechnology, vol. 21, Apr 9 2010.

[15] Z. Liu and M. Misra, "Dye-Sensitized Photovoltaic Wires Using Highly Ordered TiO2 Nanotube Arrays," Acs Nano, vol. 4, pp. 2196-2200, Apr 2010.

[16] R. R. Rangaraju, K. S. Raja, A. Panday, and M. Misra, "An investigation on room temperature synthesis of vertically oriented arrays of iron oxide nanotubes by anodization of iron," Electrochimica Acta, vol. 55, pp. 785-793, Jan 1 2010.

[17] S. E. John, S. K. Mohapatra, and M. Misra, "Double-Wall Anodic Titania Nanotube Arrays for Water Photooxidation," Langmuir, vol. 25, pp. 8240-8247, Jul 21 2009.

[18] Z. Liu, B. Pesic, K. S. Raja, R. R. Rangaraju, and M. Misra, "Hydrogen generation under sunlight by self ordered TiO2 nanotube arrays," International Journal of Hydrogen Energy, vol. 34, pp. 3250-3257, May 2009.

[19] S. K. Mohapatra, S. E. John, S. Banerjee, and M. Misra, "Water Photooxidation by Smooth and Ultrathin alpha-Fe2O3 Nanotube Arrays," Chemistry of Materials, vol. 21, pp. 3048-3055, Jul 28 2009.

[20] Z. Liu, V. Subramania, and M. Misra, "Vertically Oriented TiO2 Nanotube Arrays Grown on Ti Meshes for Flexible Dye-Sensitized Solar Cells," Journal of Physical Chemistry C, vol. 113, pp. 14028-14033, Aug 6 2009.

Unpublished Progress:

Technical: The following was accomplished over the last quarter.

1. Stability studies were also continued
2. Newer work on Transition metal sulfide/selenide on TiO_2 was initiated
3. Samples were also sent to Dr. Clemens Heske at UNLV for analysis
4. One peer-reviewed manuscript was published in RSC Advances
5. Two more manuscripts are under preparation for submission to Journals
6. Newer work on other transitions metals has been initiated.

SECTION 1: Newer work on Transition metal selenide on TiO_2

Abstract

Photoelectrochemical performance of CdSSe quantum dots (QDs) tethered to a framework of vertically oriented titania (TiO_2) nanotubes was studied. *Photoelectrochemical* measurements demonstrated that TiO_2/CdSSe framework has band edge structure with improved ability for charge transfer, thus validating the higher photocurrent generation. A 11-fold enhancement in photocurrent achieved with the composite film, compared to the pure TiO_2 film implies that ternary quantum dots and nanotubular structure of TiO_2 work in tandem to promote charge separation and favorably impact photoelectrochemical performance. The results suggest that structural and optoelectronic properties of TiO_2 films can significantly be improved by varying the thicknesses of CdSSe layer.

Results

UV absorption

The UV-visible light absorbance properties of TiO_2 NTA/ CdSSe(*n*) photoanodes are depicted in Fig 1. The effect of the number of deposition layers, *n* (5, 7 and 9 cycles) and post-synthesis annealing temperature (200^oC, 300^oC and 400^oC) on the optical performance of the modified electrodes has been presented and are compared with unsensitized TiO_2 NTAs (Fig. 1). Plain TiO_2 NTA film shows an absorption edge at 380 nm, corresponding to the bandgap of the anatase phase of titania.[1, 2] An additional feature appearing around ~500 nm, is a signature of anodized TiO_2 NTs and arises due to surface plasmon resonance from Ti nanoparticles trapped within nanotubes. After coupling with CdSSe QDs, the high absorption of CdSSe nanoclusters in the visible region overlaps the response due to TiO_2 and instead a broad response with absorption onset around 650 nm (for 5 cycles of deposition) was observed. With increasing deposition cycles (to 7 and 9 cycles), the absorption onset was observed red-shifted due to the size quantization effect. Annealing under N_2 atmosphere also tend to affect the optical performance of films. With annealing at 300^oC, absorption intensity increased and absorption edge experienced red shift. Moreover, with annealing at higher temperatures (400^oC), the absorption onset further shifted to longer wavelengths in all cases but the absorption intensity decreased for film with 9 deposition cycles, possibly due to the aggregation of nanocrystals. This much enhanced visible light absorption of the composite films might be attributed to the wide band gap range of CdSSe QDs from 1.6 to 2.2 eV, and demonstrates the possibility of improved photoactivity of the TiO_2 NTA/CdSSe hybrid photoanode.

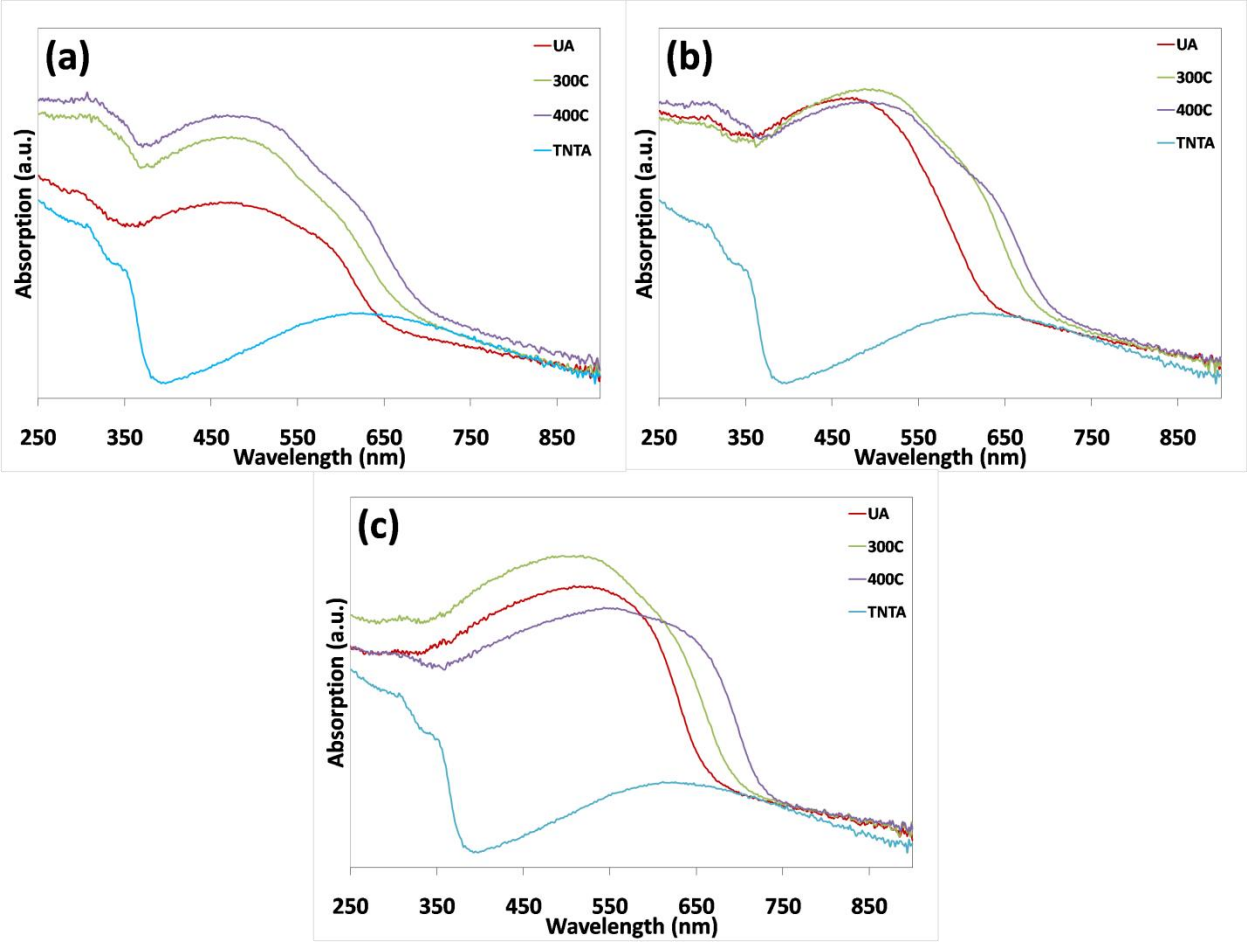

Fig.1. Absorption spectra of pure nanocrytalline TiO_2 NTA film, and the films sensitized with (a) TiO_2 NTA/ CdSSe (5); (b) TiO_2 NTA/ CdSSe (7); (c) TiO_2 NTA/ CdSSe (9); at annealing temperatures of 300^{o}C and 400^{o}C, respectively. Absorption edge was found to undergo red shift with increase in number of deposition cycles.

XRD

The XRD spectra (Fig. 2) displays the morphology of TiO_2 NTs before and after modification with CdSSe quantum dots. The peaks in the spectrum of anodized Ti foil (2A) can be indexed for underlying Ti metal (JCPDS file no. 44-1294) and TiO_2 anatase phase (JCPDS file no.: 21-1272) layer grown on the top. These peaks are labeled as 'T' and 'A' for Ti substrate and anatase TiO_2, respectively. The XRD spectrum of as-deposited TiO_2 NTA/CdSSe (9) electrode reveals the signals similar to anodized film. However, after thermal annealing under N_2, the film shows the presence of additional signals at 2θ values of 25.4^o, 42.4^o and 49.7^o, corresponding to (111), (220) and (311) planes of CdSe (JCPDS file no.: 19-0191). These results demonstrates the formation of CdSe phase only after annealing, thus resulting into a more crystalline phase. No additional S-related peak could be detected, indicating nominal amount of S inclusion within CdSe matrix.

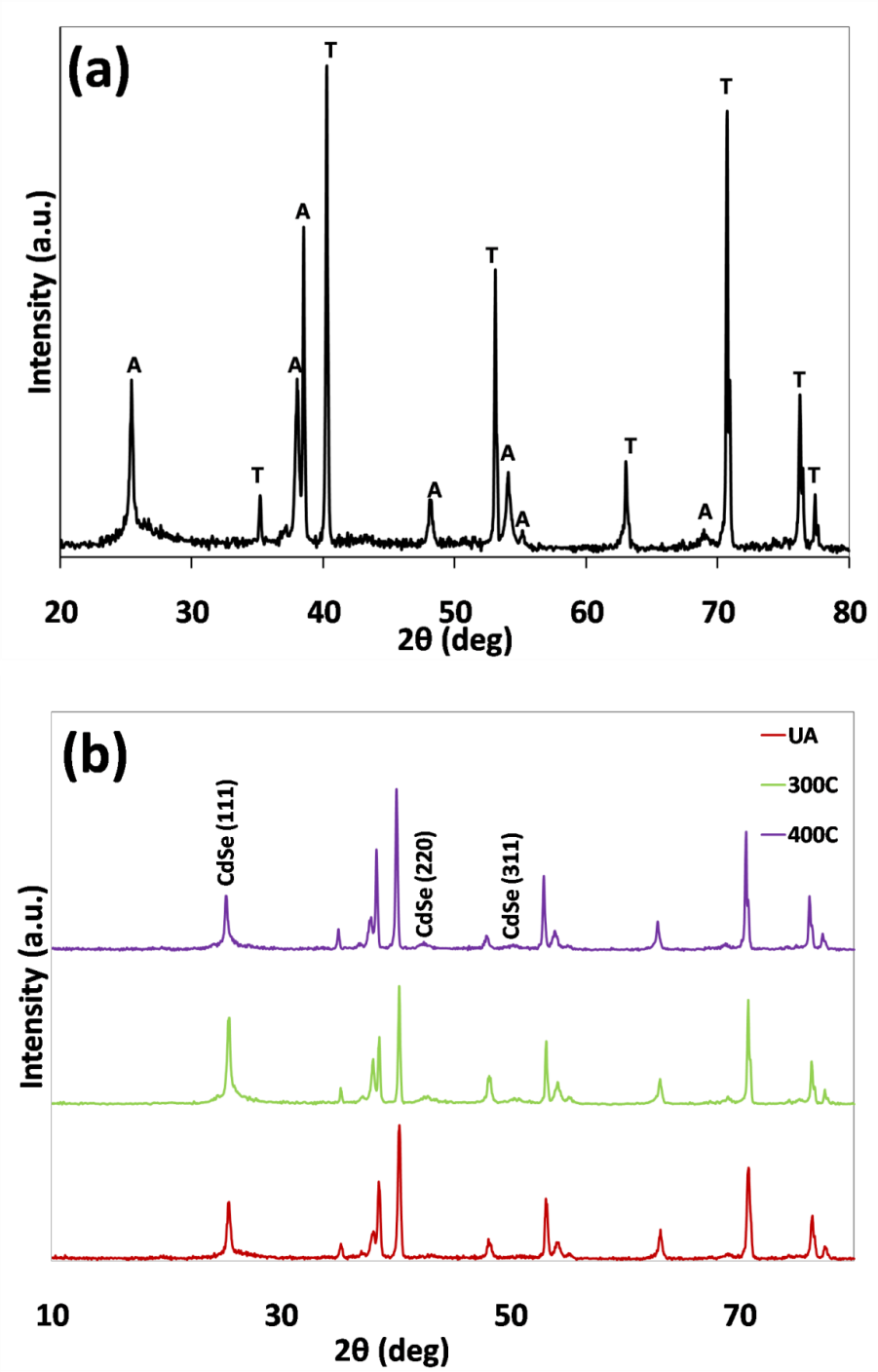

Fig. 2

Fig.2. (a) Pristine TiO2 NTAs and stacked XRD pattern of (b) TiO2 NTA/CdSSe(9) unannealed sample, and sample annealed at 400oC. The patterns reveal that CdSe phase appears after annealing. The absence of peak due to CdS indicates low concentration of S.

SEM

Fig 3 and 4 depicts the surface and cross-sectional images to highlight the morphological change of the TiO_2 nanotube array films before and after CdSSe deposition. Fig 3 shows the formation of regularly arranged grown perpendicular from the Ti foil substrate, with a wall thickness of approximately 10 nm and a mean inner-pore diameter of about 70 nm. The open structure of tubes provides superior access for sensitizer material as well as promotes unidirectional charge transport due to one dimensional feature of tubes. After QD deposition, the walls of NTs became very rough and decorated with a bunch of QD particles (as displayed in Figs. 3(a-d) and 4b), suggesting that QDs cover both the outer and inner surfaces of NT arrays, owing to the decreased resistance to mass transfer offered by the inner surface. The top view of CdSSe-sensitized NTs with different number of deposition cycles has been displayed in Figs. 3 a-d. The images clearly indicate the increasing amount of QDs loading on NTs with increasing deposition cycles. With annealing, the nanocrystals start to aggregate and form small clusters.

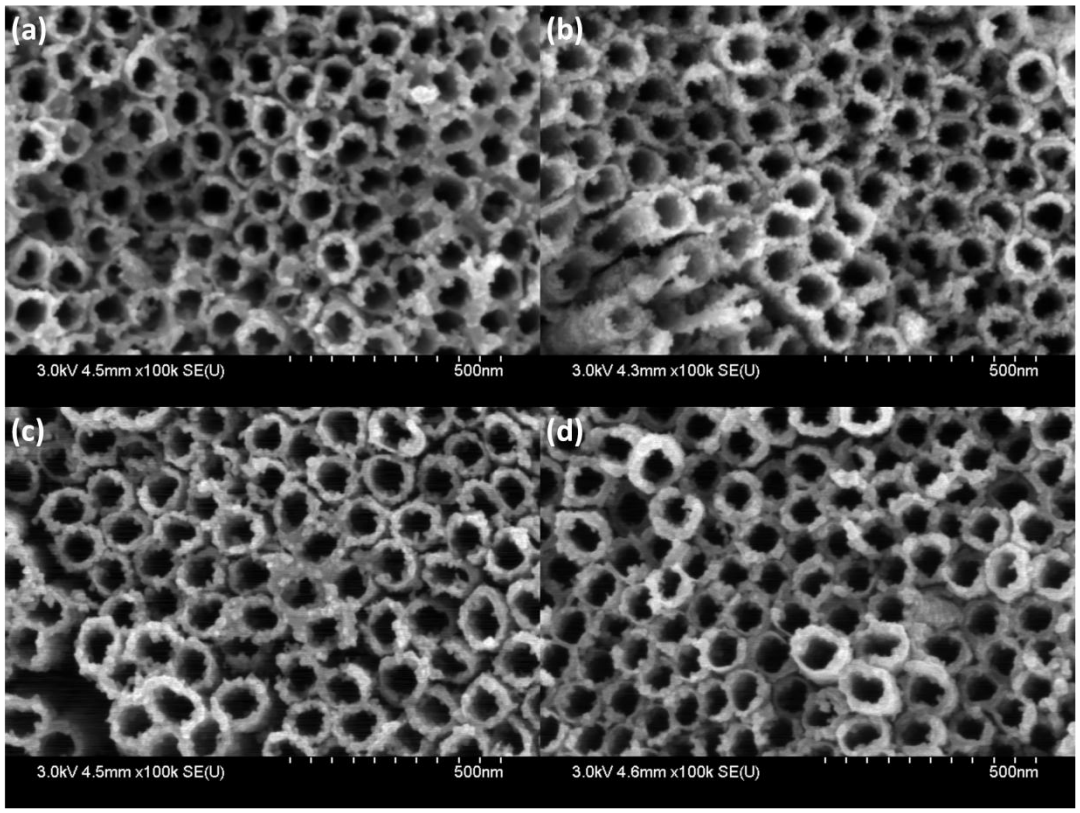

Fig. 3

Fig.3. Scanning electron microscopy images (top view) of (a) TiO2 NTA/CdSSe (7)-400oC, (b) TiO2 NTA/CdSSe(9)-UA, (c) TiO2 NTA/CdSSe(9)-300oC, (d) TiO2 NTA/CdSSe(9)-400oC. The images depict that the CdSSe nanocrystals are uniformly attached to surface of TiO2 NTAs.

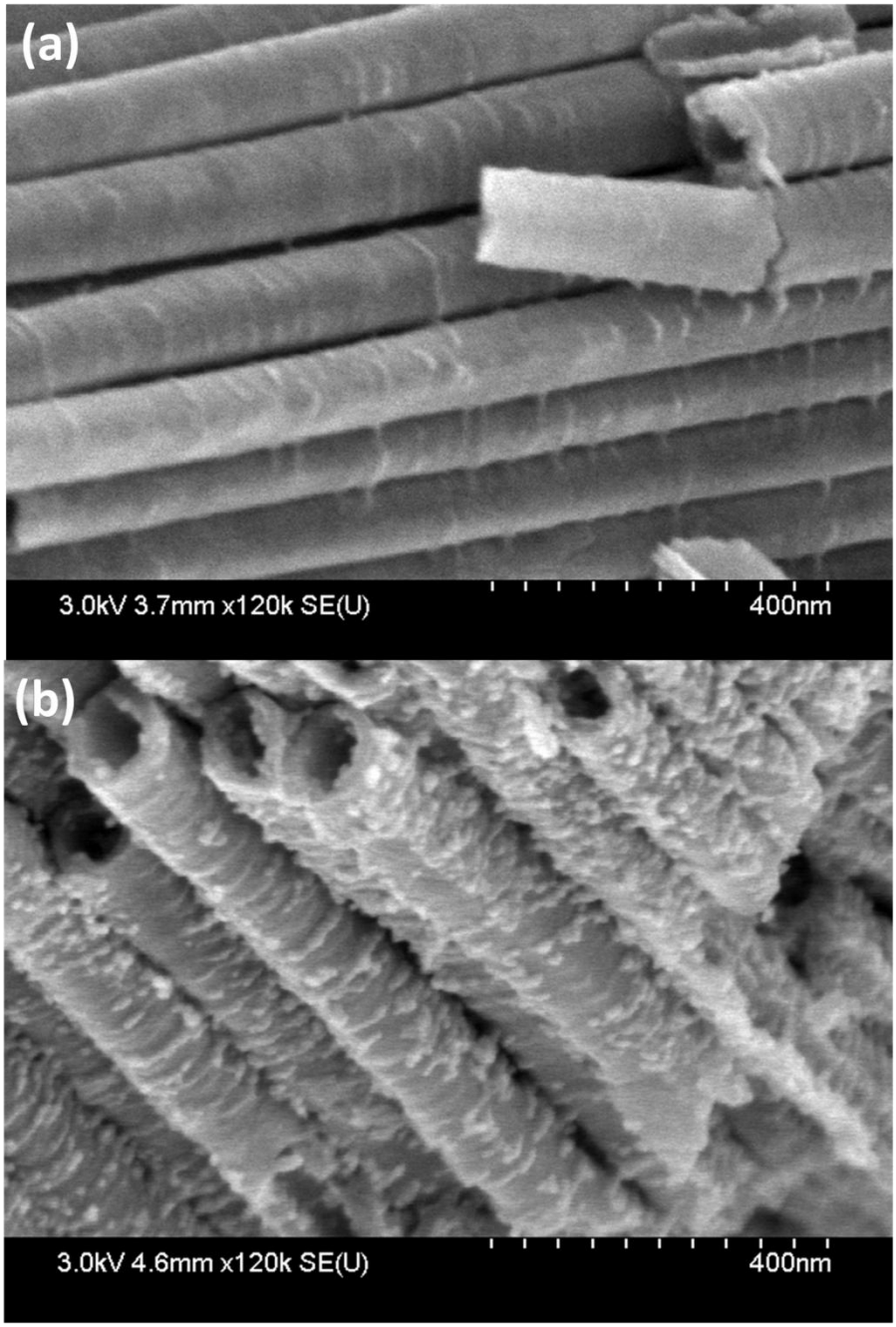

Fig. 4

Fig.4.Cross-sectional view of (a) unsensitized TiO_2 NTAs and (b) sensitized TiO_2 NTA/CdSSe (9) film. The sensitized sample was subjected to thermal treatment under nitrogen atmosphere at 400^{o}C for 1 hour. CdSSe deposits are clearly visible on the walls of nanotubes.

SECTION 2: Analyses conducted at UNLV

The goal of this project was to investigate the chemical and electronic characteristics of titanium dioxide (TiO_2) nanotubes decorated with different metals or nonmetals in order to produce highly efficient photocatalysts for the generation of hydrogen, as supplied by the project lead at the University of Nevada, Reno (UNR). The experimental plan included UNLV lab-based techniques, in particular X-ray Photoelectron Spectroscopy (XPS) to characterize the chemical state of the surface, and Ultraviolet Photoelectron Spectroscopy (UPS) and Inverse Photoemission Spectroscopy (IPES) to derive the electronic surface structure (electronic band gap, surface band edge positions, work function). To support the data interpretation, investigations into the surface morphology with Scanning Electron Microscopy (SEM) were also conducted. Furthermore, samples were investigated with X-ray absorption (XAS) and emission (XES) spectroscopy at the Advanced Light Source, Lawrence Berkeley National Lab, during our experimental campaigns within our Approved Program on Beamline 8.0.

In discussions with the project lead at UNR, it was decided that the first sample set should include non-decorated TiO_2 nanotubes that had been previously grown at UNR. These samples would allow a test and optimization of the sample handling and measurement procedures, allow first insights into the particularities of the nanotubes systems, and, after appropriate surface cleaning steps, serve as a baseline for the electronic and chemical structure of the nanotubes prior to decoration. Two samples were sent to UNLV to supply this baseline. Both samples were made using the electrochemical anodization method, but only one of the samples was subject to a final annealing step.

After the initial XPS measurements (shown in Figures 1 & 2) were taken, both samples had two small squares (3 mm^2 in size) cut out in order to take SEM measurements to support our XPS data. The larger pieces were then measured with a monochromatic x-ray source for a cleaning series with low-energy Argon ions (50 or 100 eV).

Figure 1 shows the XPS survey spectra taken with Al K_α (1486.6 eV) excitation of the as-received samples, annealed (top) and unannealed (bottom). The pertinent TiO_2 photoemission and Auger lines (Ti, O) as well as F and C lines are labeled. The surveys show that the Ti 2p and O 1s peaks are more intense for the annealed sample, while the C 1s peaks are comparable with each other. The surveys also show that F is found only on the unannealed sample.

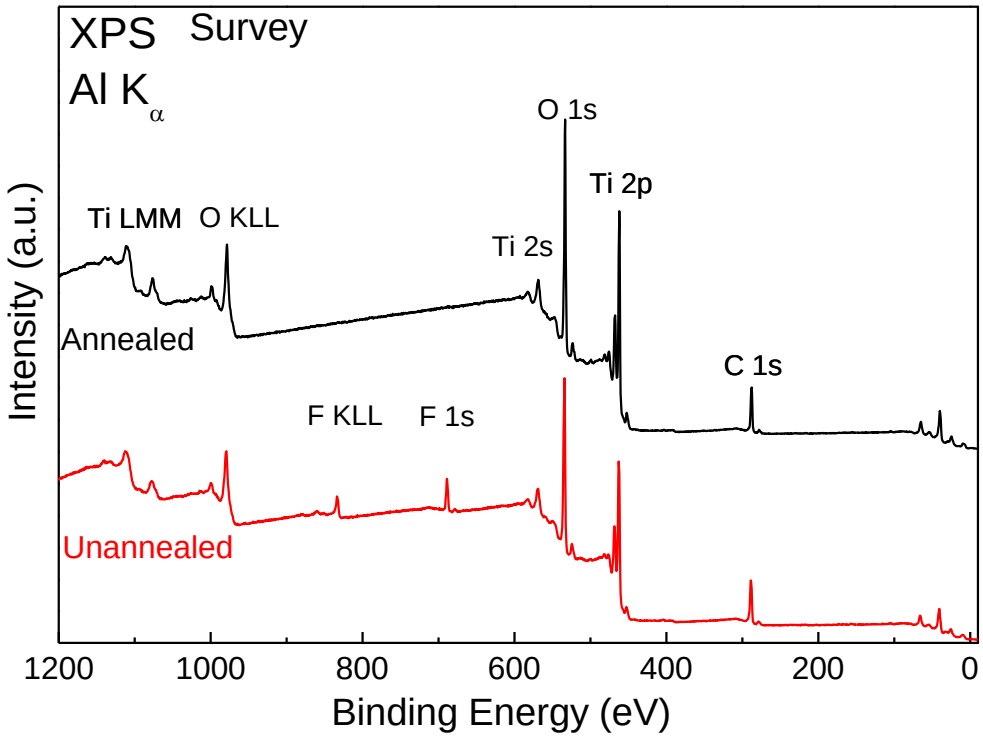

Figure 1: Al K_α XPS survey spectra of annealed and unannealed TiO_2 nanotubes grown on Ti foil.

After exposure to x-ray irradiation, the samples turned black. To better understand this observation, SEM images were taken to compare the non-exposed to the exposed side of the TiO_2 nanotubes in order to check for beam damage, but no direct evidence for beam damage could be found in either the SEM or additional XPS spectra (not shown).

In order to further understand the spectral differences between the annealed and unannealed samples, Figure 2 shows two SEM images of the two samples (in a region that was exposed to x-ray irradiation during the XPS measurements). In addition to checking for beam damage, the SEM was also used to get an idea of the overall sample morphology to aid in the analysis of the XPS spectra (e.g., the possible origin of the C signal). Figure 3 shows an SEM image of the annealed sample (in a region previously exposed to x-rays irradiation). It shows layers of nanotubes lying on top of each other, suggesting that the carbon signal observed in XPS could be coming from both, adsorbates on the surface of the film (e.g., due to air exposure), but also possibly from carbon embedded in or between the tubes.

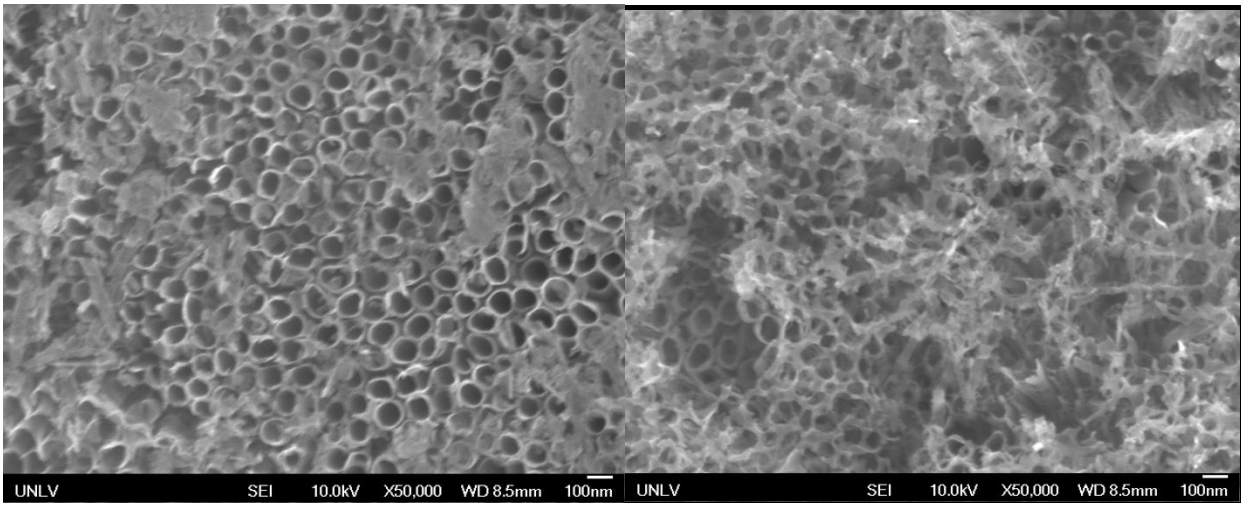

Figure 2: SEM images taken at a magnification of 50,000 of unannealed (left) and annealed (right) TiO_2 nanotubes grown on Ti foil.

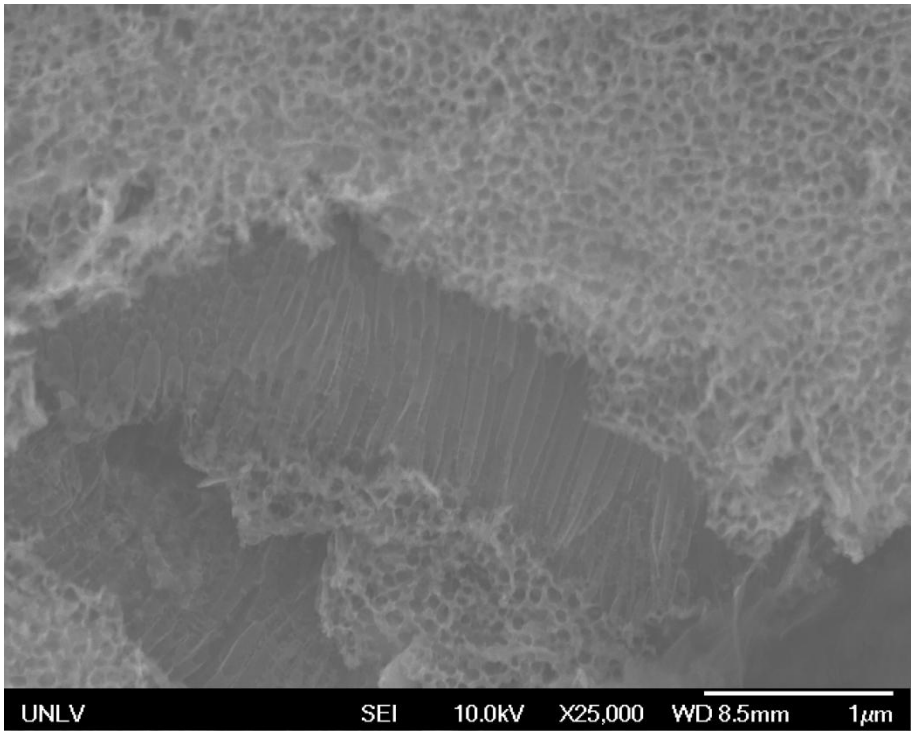

Figure 3: SEM image taken at a magnification of 25,000 of annealed TiO_2 nanotubes grown on Ti foil after being exposed to X-ray irradiation.

In the following, we will discuss a first surface-cleaning series, using low-energy Ar ions (50 eV and 100 eV). The cleaning series was done in several steps. First, a set of XPS measurements was taken to see if the samples had changed while being stored in the glovebox after the first set of measurements. Then, the cleaning series was started using 50 eV ions for two sets of 10 min and one 20 min exposure (total of 40 min). After this, 100 eV ions were used and the sample was exposed for 20 min. After each cleaning step, XPS spectra were taken to observe possible changes.

Figure 4 shows the XPS survey spectra taken with monochromatic Al K_α excitation of the annealed sample, before the cleaning (black) and after the final cleaning step (red). The pertinent TiO_2 photoemission and Auger lines (Ti, O) as well as the peaks associated with C are labeled. The surveys show that the Ti 2p and O 1s peaks are more intense after cleaning, while the C 1s peak has decreased after cleaning, as expected. However, the applied treatments are not sufficient to remove the carbon signal fully.

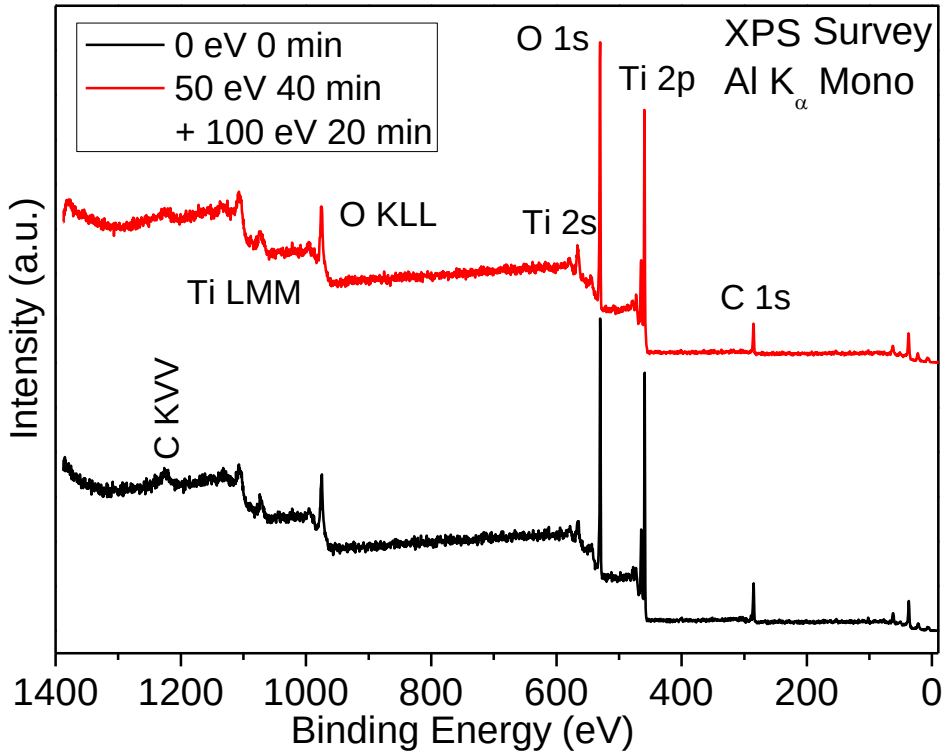

Figure 4: XPS survey spectra (taken with monochromatized Al K_α excitation) of the annealed TiO_2 nanotube sample before and after a series of ion cleaning steps.

Figure 5 shows detail spectra of the C 1s and O 1s peaks of the annealed sample after every step of the cleaning series. The detailed spectra of the C 1s peaks were normalized by their background at lower binding energy, and show that the first step in the cleaning series is most effective in removing the surface adsorbates. The next 3 cleaning steps show no change in the intensity of the C 1s peak. This prompted us to use higher-energy ions for the next step. In this last step, some of the C remaining after the 50 eV ion treatments is indeed removed from the surface.

The detailed spectra of the O 1s peaks have also been normalized by their background, and show that the first step in the cleaning series results in a slight increase in the intensity of the peak. This is due to the decrease in surface adsorbates (indicated by the C intensity decrease), which exposes more of the TiO_2 nanotubes. However, the successive cleaning steps show a decrease in the O 1s intensity. Since the C 1s spectra are not changing after the first cleaning step, the decrease in O intensity might be an indicator that the nanotubes are damaged by the low-energy ions.

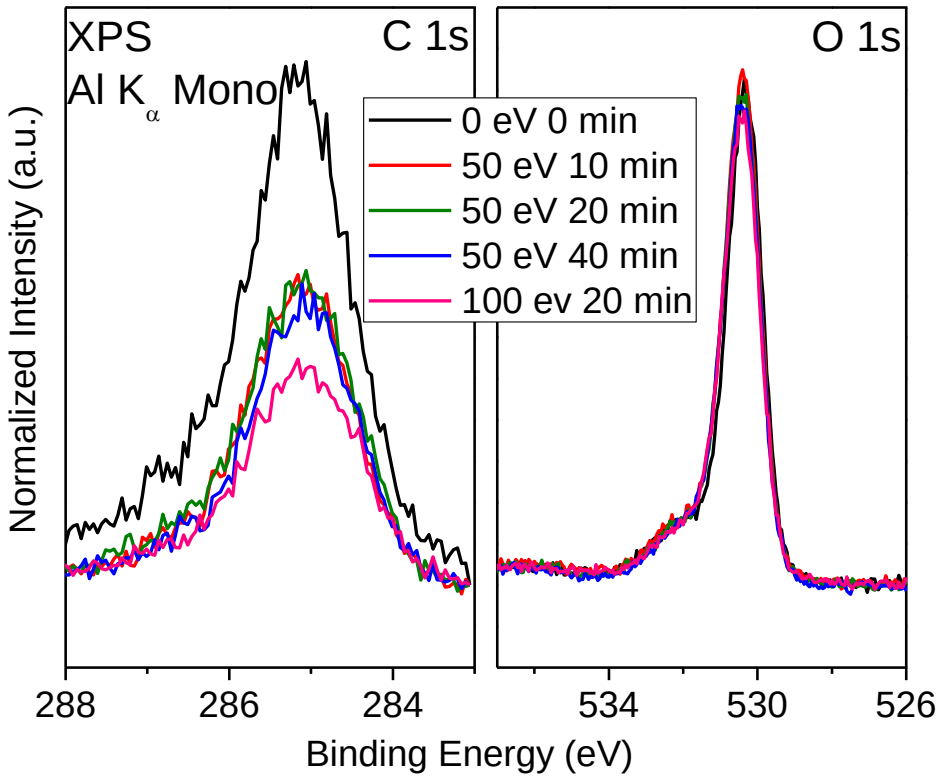

Figure 5: Detail XPS spectra of the C 1s and O 1s peaks of annealed TiO_2 nanotubes after several cleaning steps using low-energy Ar ions. The peaks were normalized to their respective backgrounds at lower binding energy.

Figure 6 shows detailed spectra of the Ti 2p peaks of the annealed sample after every step of the cleaning series. The detailed spectra of the Ti 2p peaks were normalized by their peak height. This normalization is well suited for showing changes in the lineshape and hence the chemical environment of the Ti atoms. The arrow in Figure 6 shows that with successive exposures to Argon ions, a shoulder is emerging at 457 eV. This shoulder is indicative of metallic Ti, most likely emerging due to damage done of the tubes by the low-energy Ar ions. This is in agreement with the finding of a reduced oxygen surface content after prolonged ion treatment.

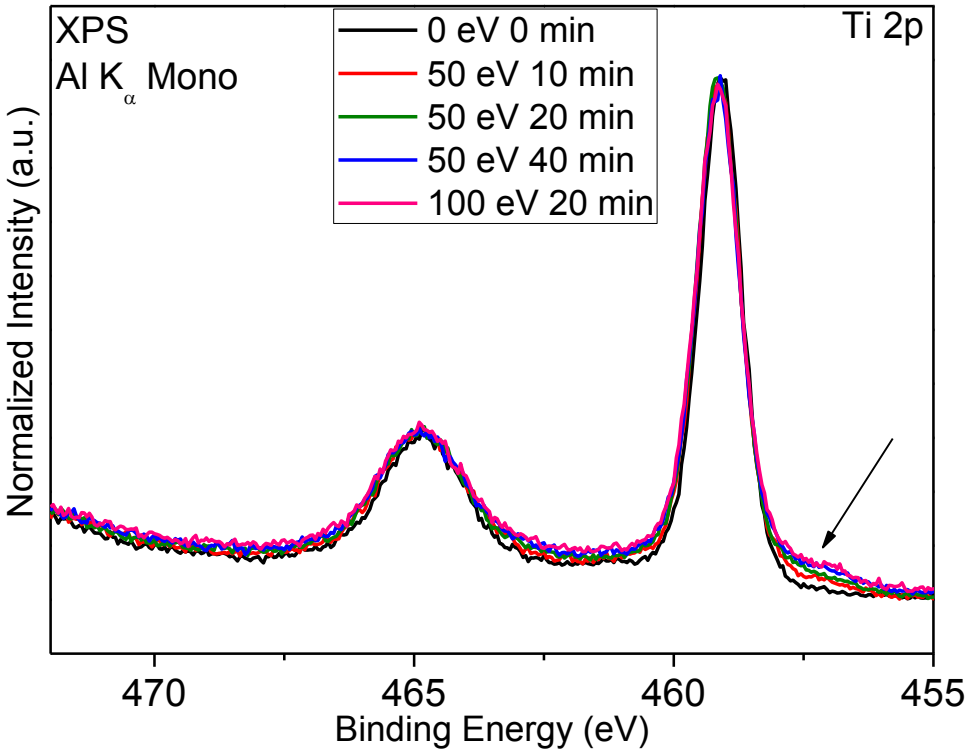

Figure 6: Detail XPS spectra (taken with monochromatized Al K_α excitation) of the Ti 2p peaks of the annealed TiO_2 nanotube sample, cleaned in steps with low-energy Ar ions. The peaks were normalized to the background and the maximal Ti $2p_{3/2}$ peak intensity.

We further investigated the electronic structure of annealed TiO_2 nanotubes grown on a Ti foil by performing XPS, UPS, and IPES measurements at UNLV, as well as XAS, XES, and RIXS measurements at the Advanced Light Source, Lawrence Berkeley National Lab. Prior to these measurements, the sample had been stored in our ultra-high vacuum (UHV) chamber for about two months; thus, the here-studied surface is the end-product of the above-reported ion treatment series using Ar ions at 50 eV (40 min) and 100 eV (20 min) (Figure 4). In addition, further surface adsorbates due to the prolonged storage in the UHV system could be present.

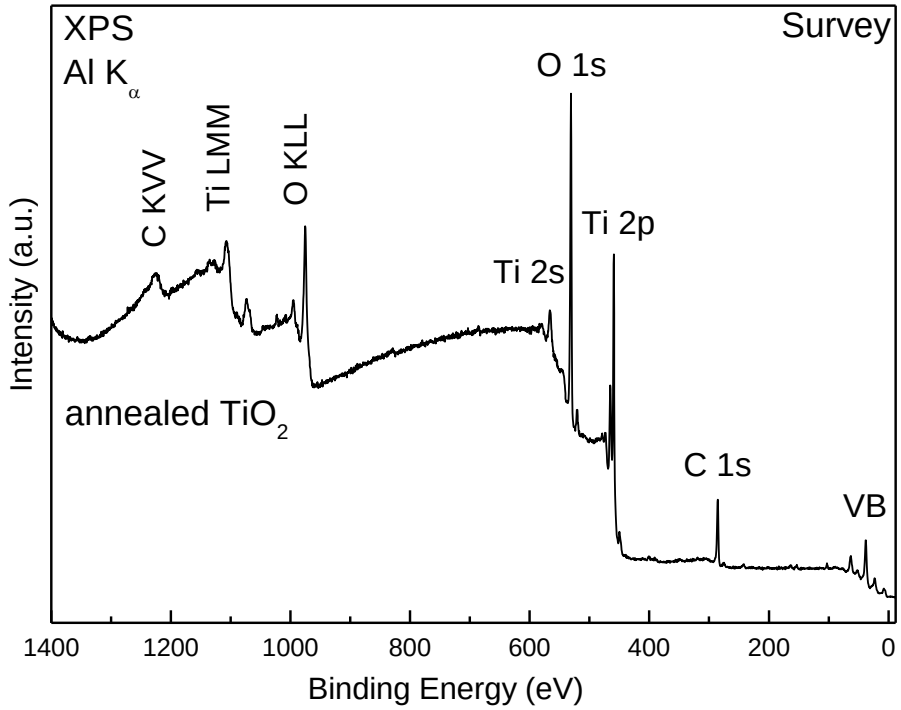

Figure 7: Al K_α XPS survey spectrum of annealed TiO_2 nanotubes grown on Ti foil (spectrum taken after a previously reported ion treatment and two months of storage in UHV).

Figure 7 shows the XPS survey spectrum taken with Al K_α excitation. The pertinent TiO_2 photoemission and Auger lines, as well as the C lines are labeled. The spectrum has not

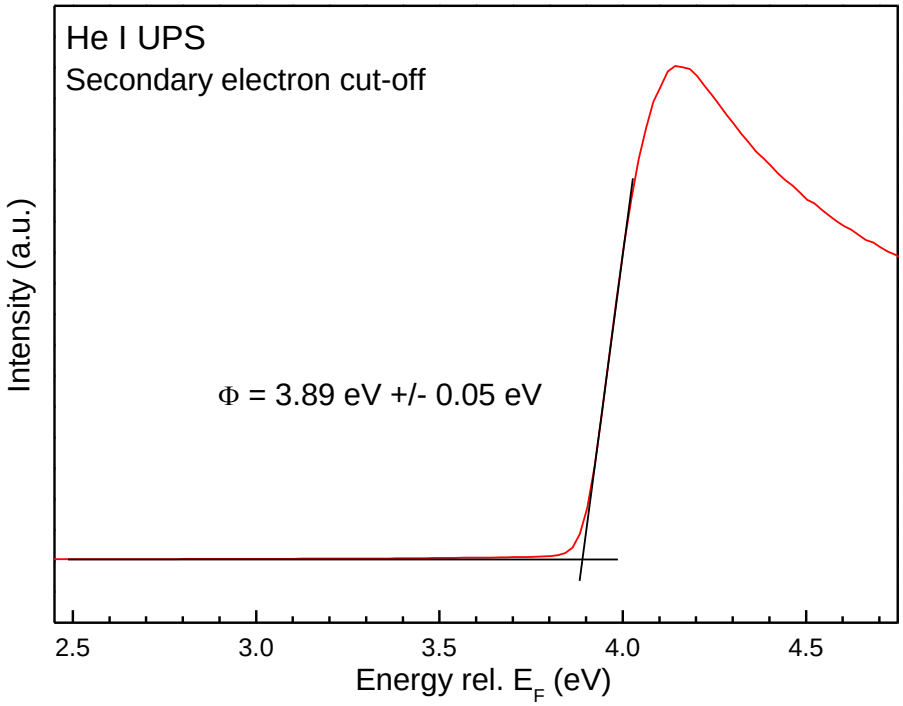

Figure 8: He I UPS secondary electron cut-off, together with linear extrapolations to determine the work function of the surface (3.89 ± 0.05 eV).

significantly changed during the two months of UHV storage, i.e., no additional contaminants such as F or N are found after storage, and the carbon signal intensity is similar to that before the storage period (when compared to the Ti 2p and O 1s peak height).

The secondary electron cut-off of the sample, as taken by He I UPS, is shown in Figure 8. The linear extrapolation of the leading edge and the low-energy baseline allows a determination of the work function (3.89 ± 0.05 eV). The work function is of large importance for aligning the electronic structure and its energy reference (i.e., the Fermi energy) with the electrochemically relevant energy scales in a PEC device. Furthermore, it represents the most sensitive measurement of the specific surface situation and is very useful for monitoring surface adsorbates and their removal.

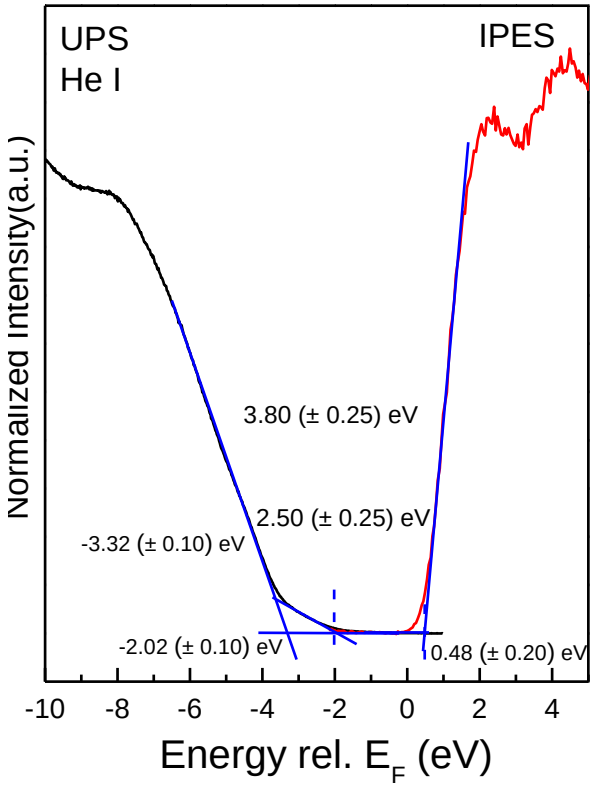

Figure 9: He I UPS (valence band, left) and IPES (conduction band, right) measurements.

Figure 9 shows combined data of UPS and IPES with respect to the Fermi energy (E_F). The valence band maximum (VBM) and conduction band minimum (CBM) are derived by linear extrapolations of the leading edges and baselines. On the valence band side, a significant foot between -2 and -3 eV complicates the analysis, because it likely includes the "true" VBM, in addition to defect states and experimental broadening. Applying the two extreme linear approximations for the VBM, we derive values of -2.0 and -3.3 eV (± 0.1 eV). For the conduction band, the spectral shape is more conclusive, and a CBM of 0.5 ± 0.2 eV is obtained. Combining both measurements, a surface electronic band gap between 2.5 and 3.8 eV (± 0.25 eV) is estimated.

In addition to the lab-based techniques, XES and XAS measurements were performed during our experimental run at the ALS in April 2014. With our SALSA end station it is possible to measure an entire RIXS (Resonant Inelastic soft X-ray Scattering) map within several minutes (O K edge, Figure 10). A RIXS map is a two-dimensional representation of the color-coded emission intensity as a function of emission (abscissa) and excitation (ordinate) energy. The emission spectrum at (non-resonant) excitation energy of 556.1 eV is shown at the top of the map, and the spectrum on the right represents a partial (518 - 531 eV) fluorescence yield absorption spectrum (which is also shown in Fig. 11). The elastically scattered peak (Rayleigh line) can be found as a

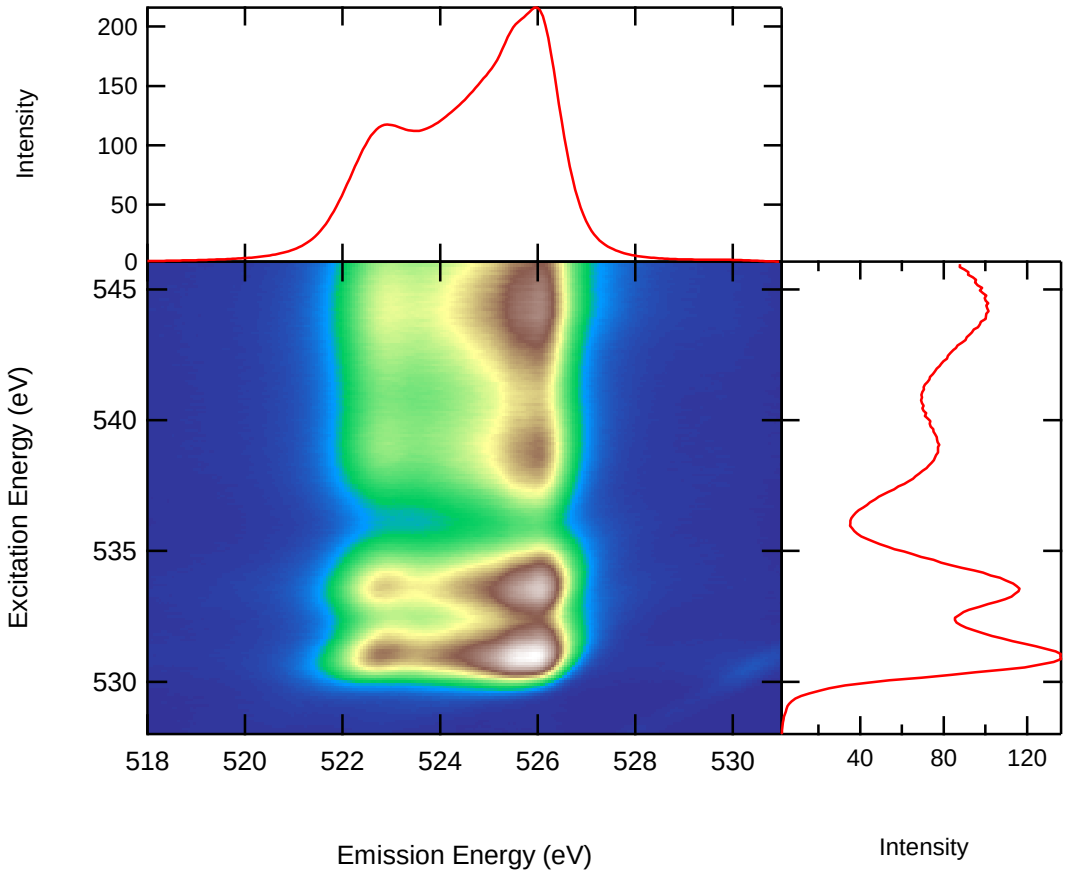

Figure 10: O K RIXS map of annealed TiO_2 nanotubes grown on Ti foil. The horizontal axis represents the emission energy, the vertical axis shows the excitation energy, and the emission intensity is color-coded (in arbitrary units). Above the map, a non-resonant spectrum (excitation energy of 556.1 eV) is shown. The right panel corresponds to a partial fluorescence yield absorption spectrum by integrating over all emission energies shown.

weak diagonal line with equal excitation and emission energies on the lower right corner of the map. These maps contain the full emission and absorption information available for a sample and hence give the most complete depiction of the underlying electronic structure.

For a first understanding of the map, the XAS spectrum and the non-resonant XES spectrum were extracted from the map and compared with reference data. Figure 11 shows the O K XAS spectra of the annealed sample, together with measurements from two TiO_2 single crystals [(100) and (001) orientation]. The low-energy range of the spectra (529 – 536 eV) is dominated by two strong broad peaks (labeled t_{2g} and e_g) that are due to the unoccupied oxygen 2p states, hybridized with the Ti 3d bands. The high-energy part of the spectrum is a result of the delocalized anti-bonding O 2p sates coupled with Ti 4s and p orbitals [F.M.F. de Groot et al., Phys. Rev. B **48**, 2074 (1993)]. Judging from the relative intensity of the two near-edge peaks, the annealed TiO_2 sample more closely resembles the TiO_2 (001) reference, while the high-energy range (above 536 eV) is not described well by either reference.

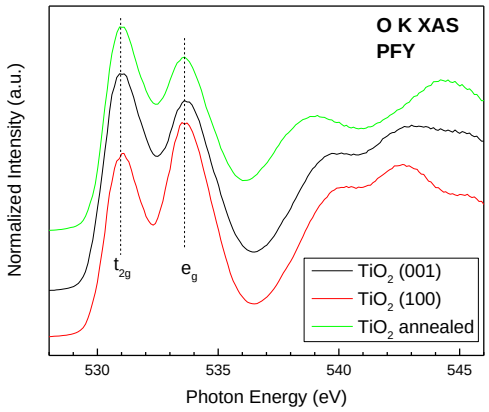

Figure 11: O K edge XAS spectra (partial fluorescence yield) of annealed TiO_2 nanotubes grown on Ti foil, and two TiO_2 single crystals [(001) and (100)].

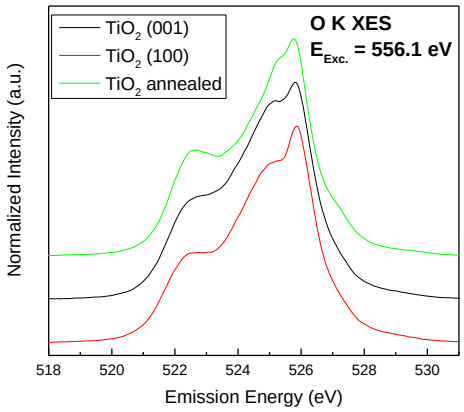

Figure 12: Non-resonant O K XES spectra of annealed TiO_2 nanotubes grown on Ti foil and two TiO_2 single crystals [(001) and (100)], excited at a photon energy of 556.1 eV.

In Figure 12, the non-resonant XES spectrum ($E_{Exc.}$ = 556.1 eV) of the annealed TiO_2 sample is shown, again compared with the two single crystal spectra. The O K emission is due to the transition of the filled O 2p valence states into the O 1s core hole and is a probe of the local chemical environment of the sample. The two reference spectra show one main peak at ~ 526 eV and two shoulders at ~525 and 522.5 eV. All three spectra differ in the intensity of the shoulder features. In particular, the annealed TiO_2 spectrum shows a more pronounced low-energy shoulder, while the shoulder at 525 eV is weaker. Further data analysis will be necessary to confirm this, and a detailed literature search as well as additional reference measurements will be required to fully ascribe these spectral differences to variations in the local environment of the probed oxygen atoms.

After the bare TiO_2 nanotubes were characterized extensively at UNLV and the ALS, we investigated the electronic structure of several differently decorated TiO_2 nanotubes on a Ti foil, as supplied by our partners at UNR. For this purpose, we performed XPS, UPS, and IPES measurements at UNLV, as well as an ion treatment (cleaning) step. Prior to these measurements, the samples had been stored in our glove box system, after being packaged according to an optimized packaging procedure that limits the amount of air exposure.

Figure 13 shows the XPS survey spectrum of MnCdSe-decorated TiO_2 nanotubes taken with Al K_α excitation. The pertinent Cd, Se, and TiO_2 photoemission and Auger lines, as well as the C lines are labeled. However, Mn photoemission and Auger lines are not seen due to fact that Mn is only present at dopant levels, rendering it below the detection limits of XPS. Figure 13 also shows a survey spectrum after a cleaning step using 50 eV Ar^+ ions for 20 minutes (red line). In comparing the two spectra, we find no significant intensity changes, including the C peak. This suggests that more cleaning steps might be needed to remove adsorbed carbon and thus be able to distinguish it from C that is incorporated into the nanotubes as part of the growth process.

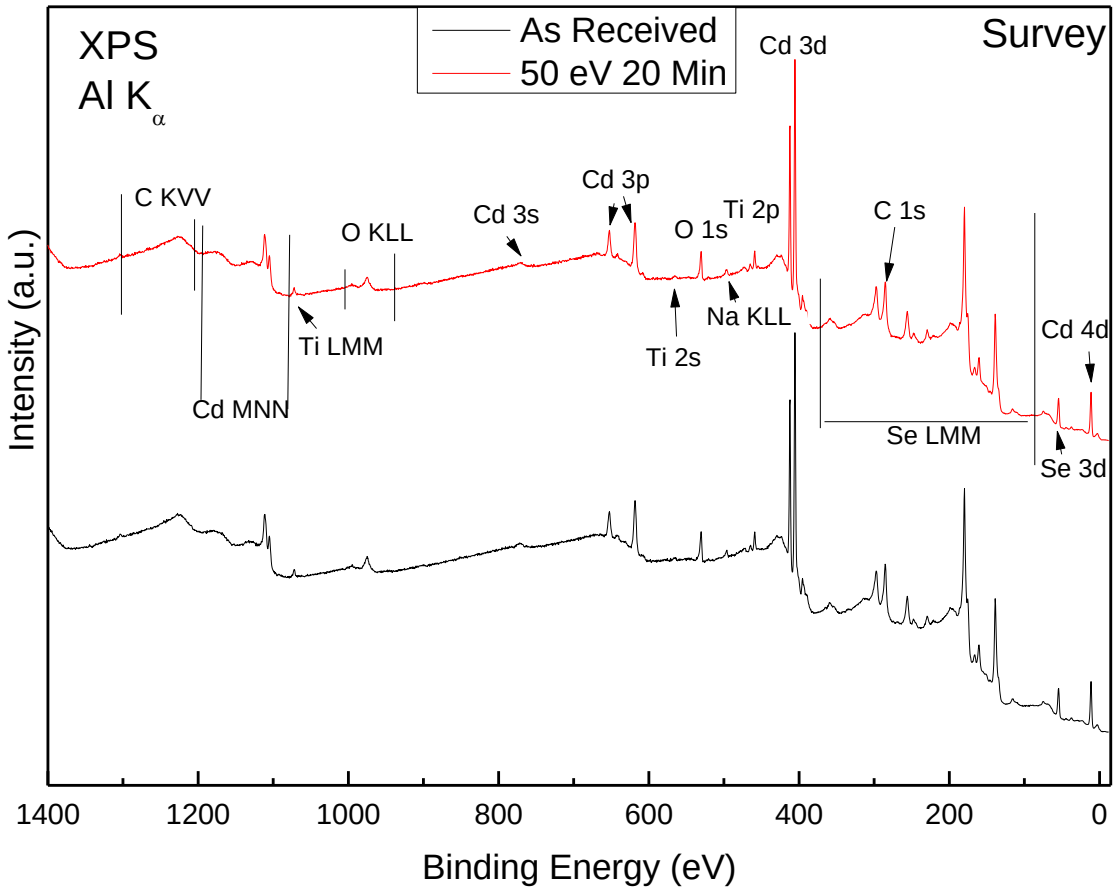

Figure 13: Al K_α XPS survey spectra of MnCdSe-decorated TiO_2 nanotubes grown on Ti foil, before ("As received") and after a 20 min cleaning step with 50 eV Ar^+ ions.

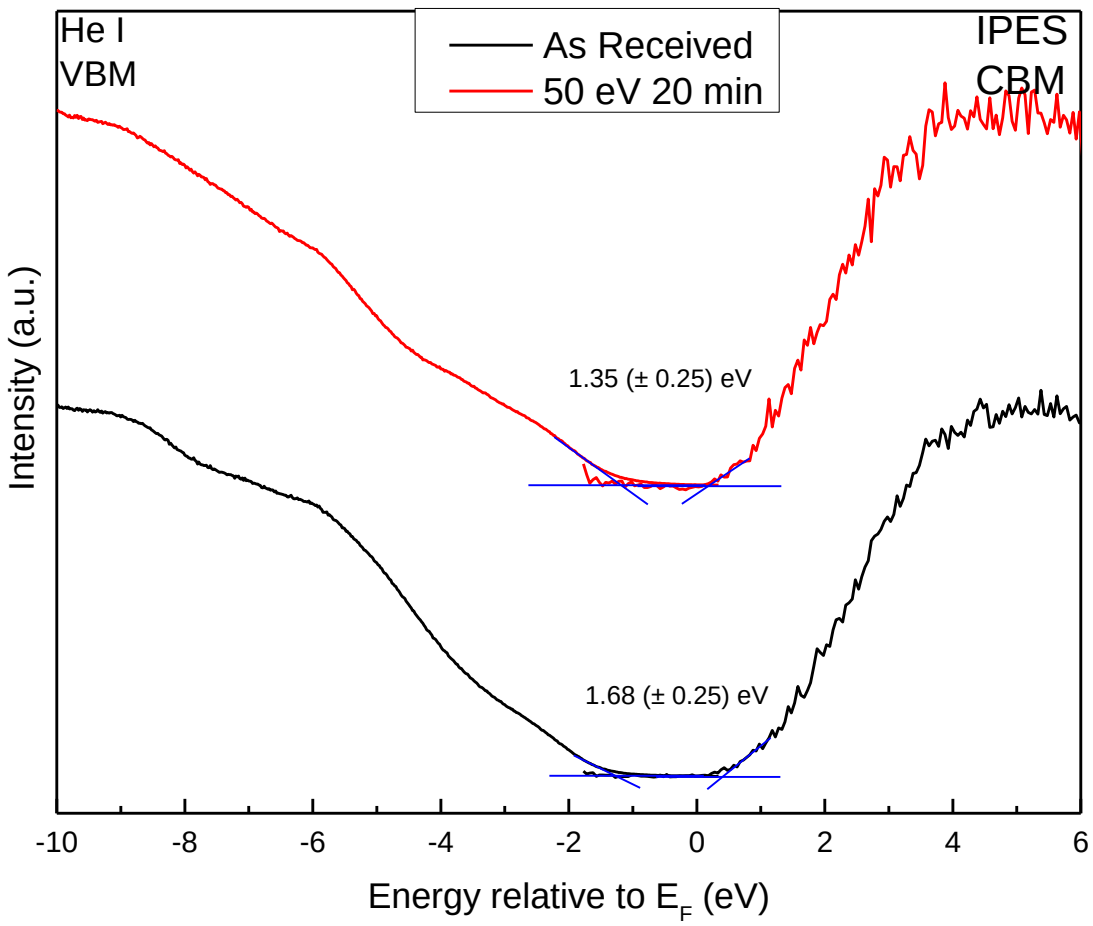

Figure 14: He I UPS (valence band, left) and IPES (conduction band, right) measurements of MnCdSe-decorated TiO_2 nanotubes grown on Ti foil.

Figure 14 shows the combined UPS and IPES data with respect to the Fermi energy (E_F) before and after the cleaning step (50 eV Ar^+, 20 min.). For the here-depicted linear approximations, an apparent surface energy separation of 1.68 eV (± 0.25 eV) and of 1.35 eV (± 0.25 eV) is determined for the as-received and ion-treated sample surfaces, respectively, in contrast to the much greater values found for the undoped TiO_2 sample shown in Figure 9. This is ascribed to a significantly reduced amount of surface contamination, as well as the impact of the MnCdSe surface decoration.

Figure 15 shows the XPS survey spectrum of ZnCdSe-decorated TiO_2 nanotubes taken with Mg K_α excitation. The pertinent Zn, Cd, Se, and TiO_2 photoemission and Auger lines, as well as the C, Na, and Cl lines are labeled. The Na peak is likely due to the use of sodium borohydride in the decoration process at UNR. In contrast, the Cl peak cannot be explained by a process step.

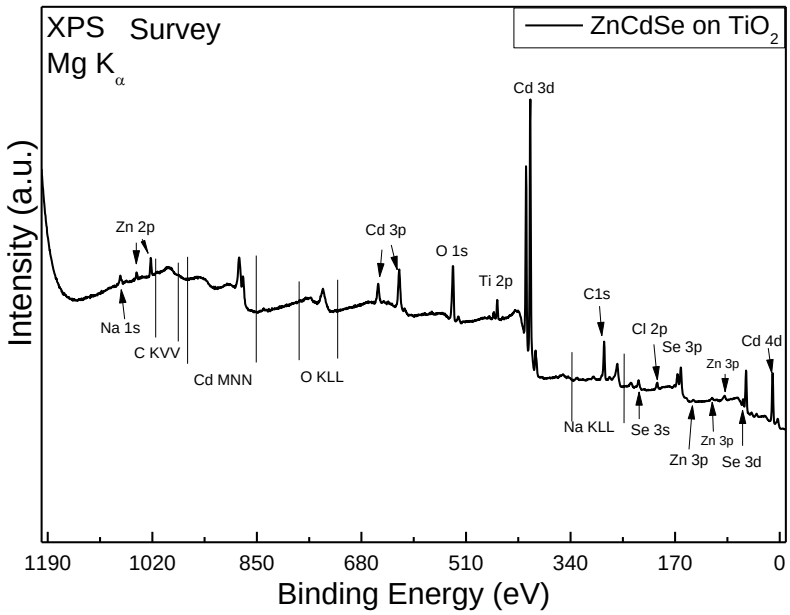

Figure 15: Mg K_α XPS survey spectra of ZnCdSe-decorated TiO_2 nanotubes grown on Ti foil.

Figure 16 shows the XPS survey spectrum of CdSSe-decorated TiO_2 nanotubes, taken with Al K_α excitation. The pertinent Cd, S, Se, Ti, and O photoemission and Auger lines, as well as the C lines, are labeled. We also find photoemission and Auger peaks associated with both Na and Cl, as for the ZnCdSe-decorated sample in Fig. 15.

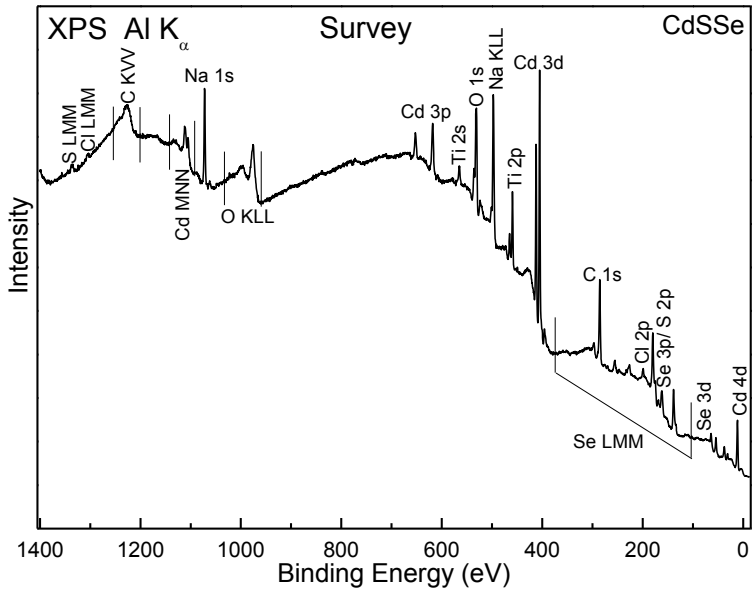

Figure 16: Al K_α XPS survey spectra of CdSSe-decorated TiO_2 nanotubes grown on Ti foil.

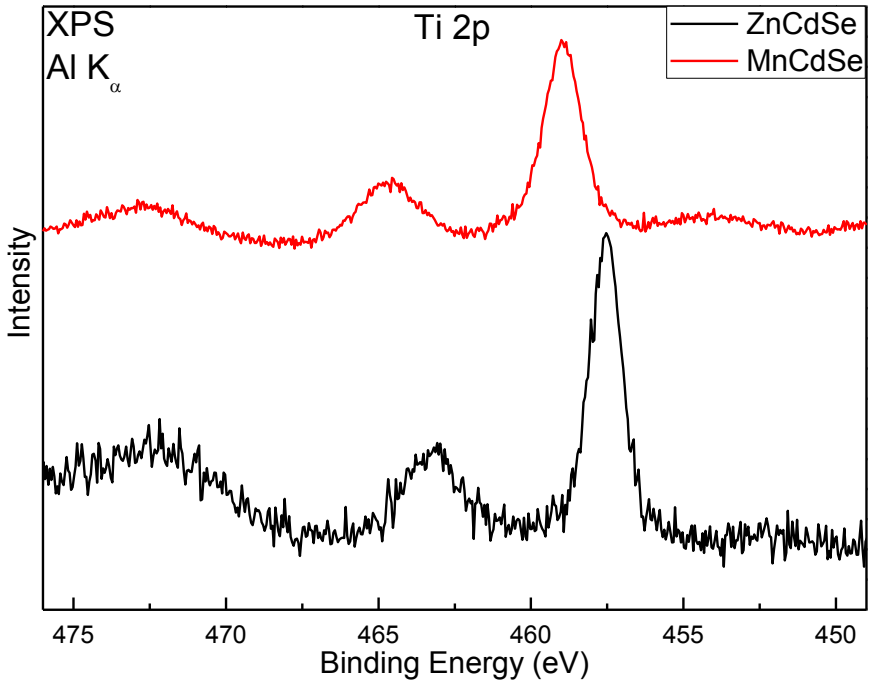

Figure 17: Al K_α XPS detail spectra of Ti 2p from both ZnCdSe- and MnCdSe-decorated TiO_2 nanotubes grown on Ti foil.

Figure 17 compares the Ti 2p photoemission peaks from both the ZnCdSe and MnCdSe-decorated samples. The shape of the Ti 2p peaks is similar, but they are approx. 1.5 eV shifted w.r.t. each other. A similar shift is found for all other core levels, as will be discussed below. Note that these spectra were recorded in two different photoemission systems, and hence additional analysis is required to ascertain that the shifts can indeed be ascribed to a different character of the two samples.

Figure 18 shows the detail spectra of the O 1s photoemission peak from both the ZnCdSe- and MnCdSe-decorated samples. Here, the shape of the O 1s peak is not similar, indicating that there are additional adsorbates and/or other oxygen-containing species on the surface of the ZnCdSe sample. A detailed fit analysis will be needed to derive the two (or more) oxygen components of the ZnCdSe-decorated sample, and to elucidate whether one of these components is also shifted by approx. 1.5 eV, as in the case of the Ti 2p peaks.

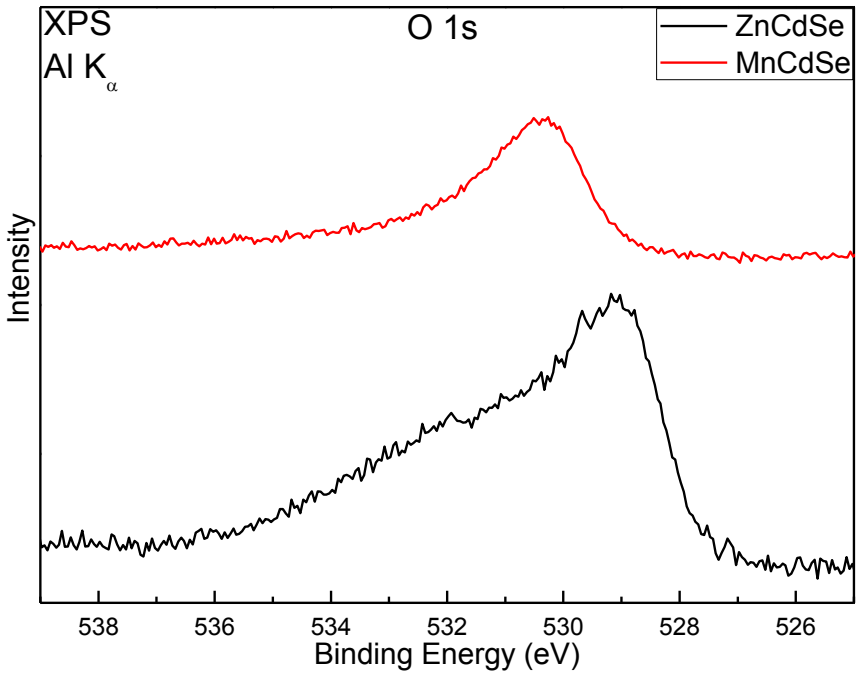

Figure 18: Al K_α XPS detail spectra of O 1s from both ZnCdSe- and MnCdSe-decorated TiO_2 nanotubes.

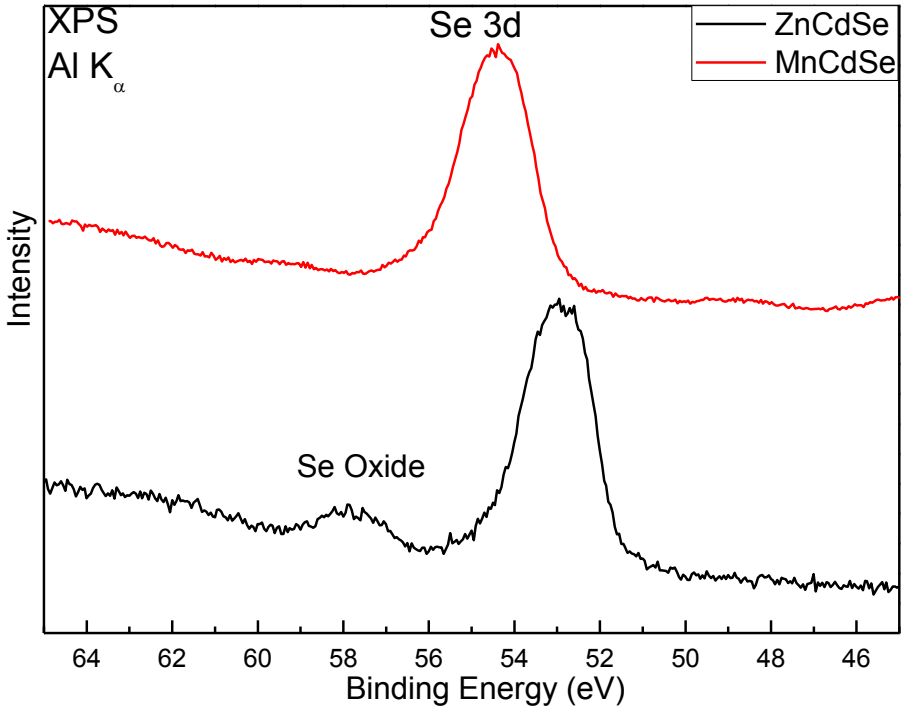

Figure 19: Al K_α XPS detail spectra of Se 3d from both ZnCdSe- and MnCdSe-decorated TiO_2 nanotubes grown on Ti foil.

Figure 19 shows the detail spectra of the Se 3d photoemission peaks from both the ZnCdSe and MnCdSe-decorated samples. Here, the shape of the Se 3d main peak is similar, while the ZnCdSe sample shows a much more pronounced selenium oxide component. This might be correlated with the additional oxygen species observed in the O 1s spectra in Fig. 18. As mentioned above in conjunction with the Ti 2p spectra, the Se 3d main peak is also shifted by approx. 1.5eV. A similar shift is also found for the Cd 3d peaks, as shown in Fig. 20.

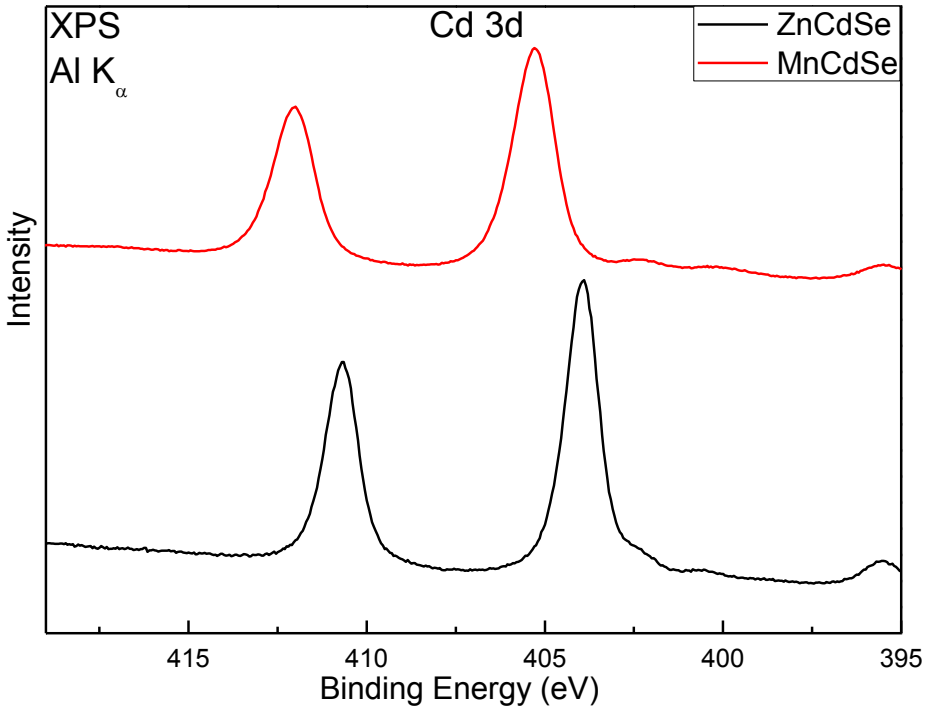

Figure 20: Al K_α XPS detailed spectrum of Cd 3d from both ZnCdSe- and MnCdSe-decorated TiO_2 nanotubes grown on Ti foil.

Figure 21 shows the detail spectra of the Cd MNN Auger peaks from both the ZnCdSe- and MnCdSe-decorated samples. The shape of the Cd MNN Auger peaks is similar and again shifted by 1.5eV w.r.t. each other. An analysis using the modified Auger parameter suggests that the Cd atoms in ZnCdSe are primarily found in an oxide environment (383.0 eV for the Cd MNN peak and 403.9 eV for the Cd $3d_{5/2}$ peak), while the modified Auger parameter for MnCdSe (381.5 eV for the Cd MNN peak and 405.3 eV for the Cd $3d_{5/2}$ peak) suggests a CdSe-like environment.

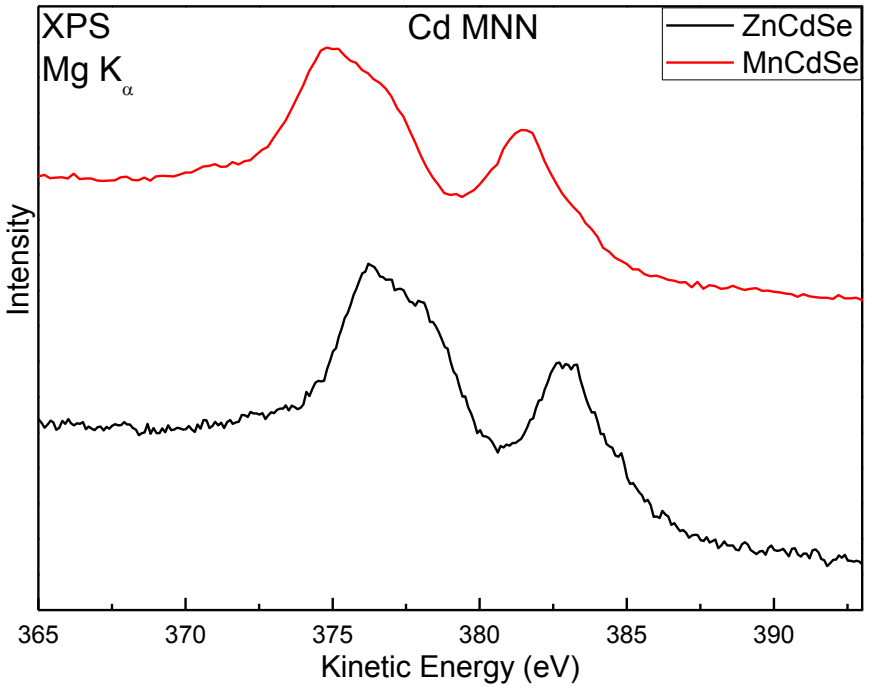

Figure 21: Mg K_α XPS detailed spectrum of the Cd MNN Auger emission from both ZnCdSe- and MnCdSe-decorated TiO_2 nanotubes grown on Ti foil.

In summary, we have used multiple techniques to characterize the electronic and chemical structure of bare TiO_2 nanotubes, TiO_2 single crystals, and several surface-decorated samples. We find that the synthesis procedures incorporate a significant amount of excess carbon and oxygen into the samples. While some of the carbon and oxygen can be removed by low-energy ion treatments, prolonged treatment lead to a modification of the chemical composition and electronic properties. RIXS maps of the bare TiO_2 nanotubes, in comparison with TiO_2 single crystals, give a comprehensive picture of the electronic structure that is significantly less affected by the surface adsorbates, and selected slices through the RIXS have been compared.

With IPES and UPS, we were able to determine the band edge positions and estimate the surface electronic band gap for the bare TiO_2 nanotubes (affected by surface adsorbates), as well as MnCdSe-decorated TiO_2 nanotubes. For the latter, a band gap of 1.35 eV (± 0.25 eV) was estimated after low-energy ion-treatment.

Lastly, we have found significant differences in the XPS data for the ZnCdSe- and MnCdSe-decorated TiO_2 nanotube samples, with the most prominent variations in overall peak position shifts (i.e., most likely, band bending modifications) as well as chemical environment; for example, an analysis of the modified Auger parameter of Cd suggests that Cd bonds to different elements (O vs. Se) within the two samples.

SECTION 3: Newer work on other transitions metals has been initiated.

Effect of cobalt catalysts on molybdenum doped BiVO4 photoelectrodes for photoelectrochemical water oxidation

Surface characterization

The surface morphology of the as-synthesized molybdenum doped $BiVO_4$ electrodes was analyzed using scanning electron microscopy. (SEM). SEM images of representative doped $BiVO_4$ films synthesized using spray pyrolysis method are shown in Fig. 1. The film consisted of several pores throughout the $BiVO_4$ film. It is well-known that the presence of the porous structure in the photoelectrodes provides an increased electrode/electrolyte interfacial area. This characteristic feature of the porous photoelectrodes helps to enhance the water splitting efficiency as the photogenerated holes will have to traverse less bulk material to be collected at the electrolyte interface and thus has a lower chance of recombining before participating in the electrochemical reaction.

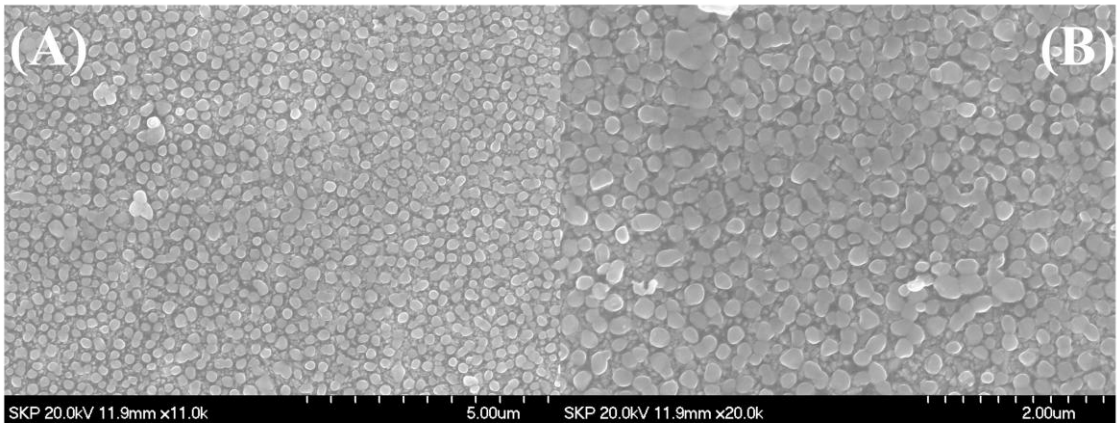

Fig. 1 SEM images of the as-synthesized molybdenum doped $BiVO_4$ electrodes at different magnifications.

In order to get additional insights into the chemical composition of the as-synthesized doped $BiVO_4$ photoelectrodes, X-ray photoelectron spectroscopy analysis was performed and the obtained results are shown in the Fig. 2. The high resolution XPS spectra for representative

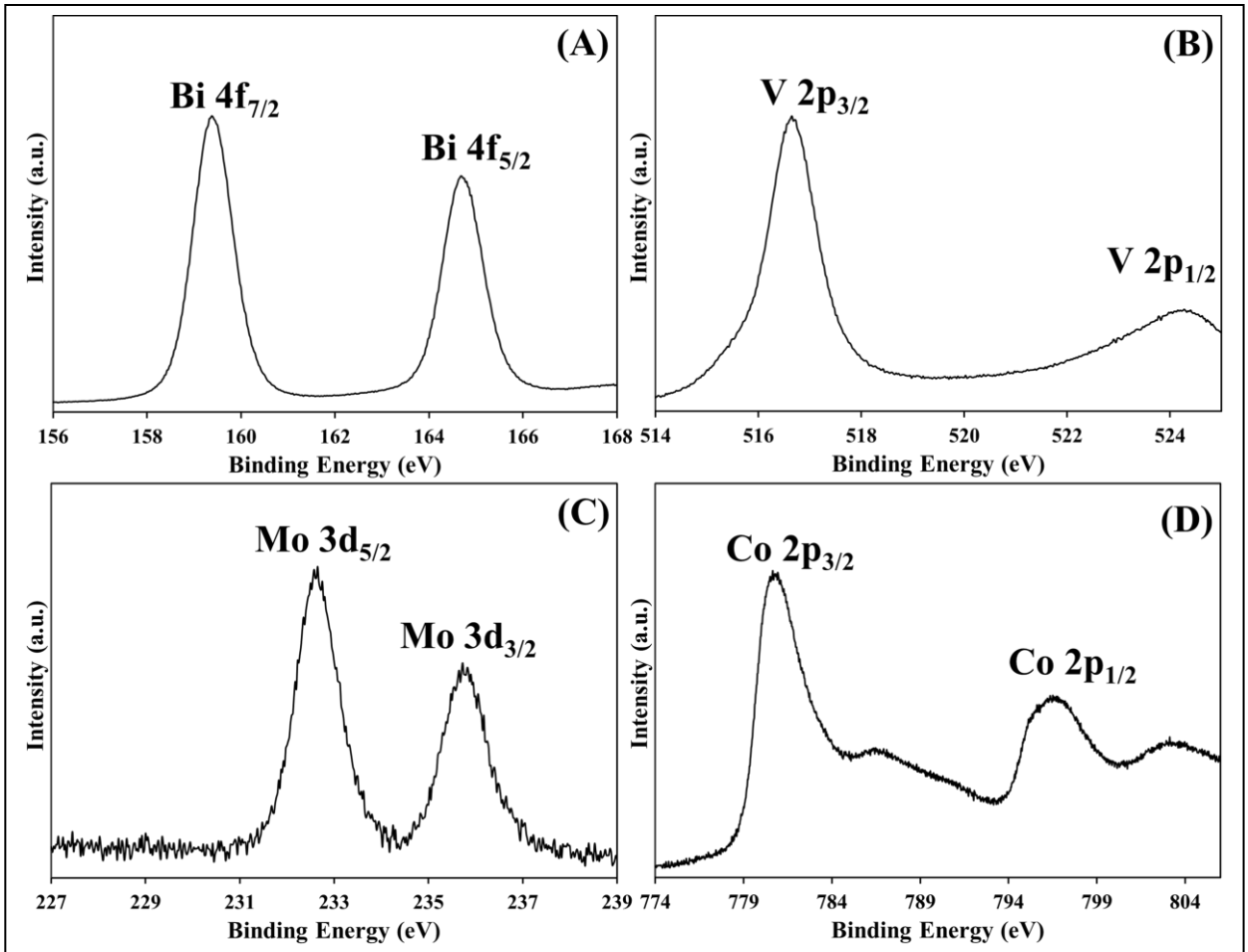

Fig. 2 XPS spectra of W doped $BiVO_4$ photoelectrodes in (A) Bi 4f; (B) V 2p; (C) O 1s and (D) Co 2p regions.

molybdenum doped $BiVO_4$/FTO electrode in the Bi 4f (Fig. 2a), V 2p (Fig. 2b), O 1s (Fig. 2c) and Mo 3d (Fig. 2d) binding energy regions exhibits the characteristic spin-orbit split of the $Bi4f_{5/2}$ and $Bi4f_{7/2}$ signals (Fig. 2a) and $V2p_{1/2}$ and $V\ 2p_{3/2}$ signals (Fig. 2b) of trivalent Bi and pentavalent vanadium respectively corresponding to that of monoclinic scheelite $BiVO_4$.[3] The $Bi4f_{7/2}$ and $Bi\ 4f_{5/2}$ peaks located at 164.7 and 159.4 eV respectively confirmed the presence of Bi^{3+} cations in doped $BiVO_4$ electrode. The split peaks of V2p were observed at 524 and 516.3 eV corresponding to $V2p_{1/2}$ and $V2p_{3/2}$ orbits respectively (Fig. 2b). In addition, the presence of signals corresponding to that of Mo $3d_{5/2}$ and $3d_{3/2}$ confirmed the presence of Mo dopant on the photoelectrode surface.

Oxygen evolution catalyst integration

A cobalt based oxygen evolution catalyst (OEC) was electrodeposited onto as synthesized molybdenum doped $BiVO_4$ electrodes by photoassisted electrodeposition method at neutral pH conditions. A three electrode cell was employed with doped $BiVO_4$, Ag/AgCl and Pt wire as working, reference and counter electrodes respectively. Cobalt based OEC films were deposited on molybdenum doped $BiVO_4$ electrodes by applying a constant potential of 0.6 V vs. Ag/AgCl for 5 min with a Gamry® rerence 600 potentiostat/galvanostat. A simulated AM 1.5 light (~ 1 sun) was employed to irradiate the semiconductor electrodes from a 300 W Xe arc lamp.

In order to understand the chemical composition of the deposited Co OECs on the surface, XPS analysis was performed on Co-OEC/Mo-dopeed $BiVO_4$ and the obtained results are shown in Fig. 2D. The cobalt spectrum of the photodeposited $BiV_{0.98}$ $Mo_{0.02}O_4$/FTO sample shows two main bands of Co $2p_{3/2}$ and Co $2p_{1/2}$ at around 781 and 797 eV originating from Co^{2+} and Co^{3+} respectively, indicting the presence of cobalt catalytic active sites on the surface of the molybdenum doped $BiVO_4$ photoelectrode.

Photoelectrochemical measurements

The PEC measurements were conducted using a Gamry® reference 600 galvanostat/potentiostat. Doped $BiVO_4$ or Co OEC integrated molybdenum doped $BiVO_4$ electrodes, Ag/AgCl and Pt wire were utilized as working, reference and counter electrodes respectively. A 300 W Xe lamp solar simulator supplied by Newport was employed to illuminate the photoanodes with 100 mW/cm^2 intensity under standard AM 1.5 (1 sun intensity) illumination**.** The light intensity was measured using Newport Thermopile Sensor 919P-003-10, 3W, 10 mm aperture. The effect of photodeposited Co-OEC on the PEC water oxidation characteristics of doped $BiVO_4$ was investigated by comparing the photocurrent responses of the molybedenum doped $BiVO_4$ photoelectrodes with and without Co-OEC. Typical current vs. potential results under chopped light illumination are shown in Fig. 3. Both electrodes exhibited anodic photocurrents upon illumination indicating the n-type nature of electrodes.

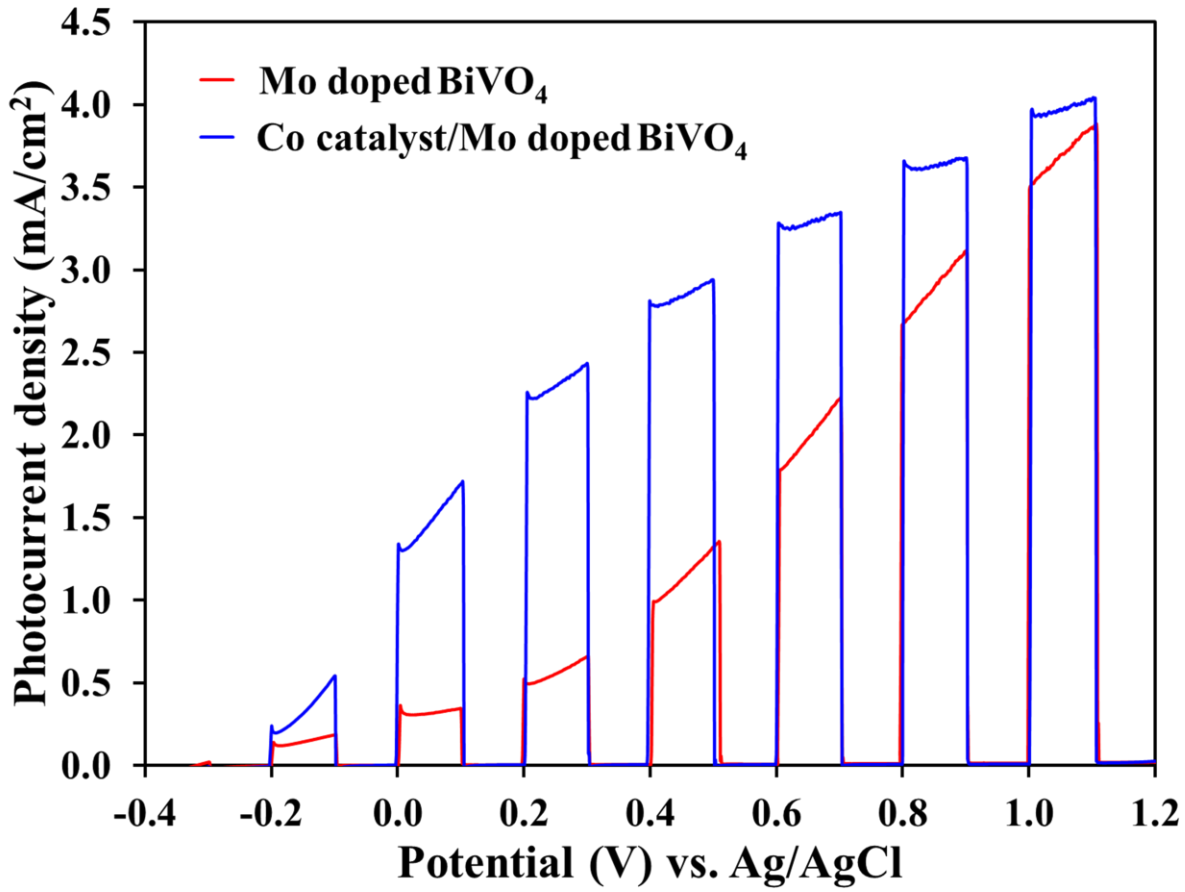

Fig. 3 Photocurrent-potential characteristics of Co-OEC/molybdenum doped $BiVO_4$ (blue) and molybdenum doped $BiVO_4$ (red) electrodes (scan rate 15 mV/s) with chopped light illumination using a 300 W Xe arc lamp (100 mW/cm^2).

The photocurrents of Co-OEC integrated doped $BiVO_4$ electrodes have been significantly enhanced when compared to the uncatalyzed $BiVO_4$ electrodes. In addition, the photocurrent has been significantly enhanced at lower applied potential region for cobalt-OEC modified electrodes and this suggests that the OER kinetics were significantly enhanced in the presence of Co-OEC.

References

[1] W.-J. Yin, H. Tang, S.-H. Wei, M.M. Al-Jassim, J. Turner, Y. Yan, Physical Review B 82 (2010) 045106.

[2] X.-F. Gao, H.-B. Li, W.-T. Sun, Q. Chen, F.-Q. Tang, L.-M. Peng, The Journal of Physical Chemistry C 113 (2009) 7531-7535.

[3] L. Zhang, D.R. Chen, X.L. Jiao, J Phys Chem B 110 (2006) 2668-2673.